

# A spectral vanishing viscosity method for stabilizing viscoelastic flows

X. Ma, V. Symeonidis, G.E. Karniadakis\*

*Division of Applied Mathematics, Center for Fluid Mechanics, Brown University,  
182 George Street, Box F, Providence, RI 02912, USA*

Received 13 September 2002; received in revised form 24 March 2003

---

## Abstract

A new method for stabilizing viscoelastic flows is proposed suitable for high-order discretizations. It employs a mode-dependent diffusion operator that guarantees monotonicity while maintaining the formal accuracy of the discretization. Other features of the method are: a high-order time-splitting scheme, modal spectral element expansions on a single grid, and the use of a finitely extensible non-linear elastic-Peterlin (FENE-P) model. The convergence of the method is established through analytic examples and benchmark problems in two and three dimensions, and unsteady flow past a three-dimensional (3D) ellipsoid is studied at high Reynolds number.

© 2003 Elsevier B.V. All rights reserved.

*Keywords:* Spectral methods; FENE-P; Numerical diffusion; Unsteady flow

---

## 1. Introduction

There has been substantial progress in the development of high-order methods and specifically spectral methods for viscoelastic flows started with the work of [1]; see, for example [2] and references therein. However, complex-geometry flows and high Weissenberg and Reynolds number regimes still present formidable difficulties. The loss of monotonicity of the solution of the stress field for many viscoelastic models becomes an even greater challenge for high-order methods. However, new ideas developed in the context of aerodynamic flows, e.g. discontinuous Galerkin methods and new stabilization techniques, have provided a new framework for developing robust high-order solvers for viscoelastic flows in complex-geometry domains. Another effective approach demonstrated in [3,4] is the use of Lagrangian and semi-Lagrangian methods that provide high-order accuracy and enhanced stability.

---

\* Corresponding author. Fax: +1-401-863-3369.

*E-mail address:* gk@dam.brown.edu (G.E. Karniadakis).

Recent studies by Fan et al. with *hp* finite elements [5] have examined standard benchmark problems using the *streamline upwind Petrov–Galerkin* (SUPG) technique combined with three different formulations: the *elastic viscous split stress* (EVSS), the *discrete* EVSS (DEVSS) and a third one, called MIX1, which proves to be very efficient in computational resources. Chauvière and Owens [6] have also used the SUPG in conjunction with features of discontinuous Galerkin methods (the SUPG–EE *element-by-element* method) for a variety of models. These include macroscopic models such as the Oldroyd-B, the finitely extensible non-linear elastic–Peterlin (FENE-P) and the Phan–Thien–Tanner (PTT) model, but also mesoscopic models such as the FENE model [7] that do not possess closed-form constitutive equations.

The dumbbell model has been in the center of viscoelastic studies due to its physical significance. The model suggests that dilute polymeric solutions are a mixture of the solvent and the polymer, where the solvent can stretch and convect the polymer molecules that are assumed to behave like elastic springs. In the limiting case of the spring being able to be stretched infinitely, the model becomes the simpler macroscopic Oldroyd-B model (or Hookean dumbbell model), which is less physical. A non-linearity was introduced first by Warner [8] to assign a maximum value to the extensibility of the spring, thus resulting to the FENE model. This model cannot be considered macroscopic, as stated above, but the modified *ensemble-averaged* FENE model, known as FENE-P, can. This model has been extensively studied by van Heel et al. [9], where they proposed a slight modification of the original model. Beris and co-workers [10,11] have also used the model to demonstrate turbulent drag reduction.

In this work we will examine the standard FENE-P model as it appears in the literature and with some small scaling variations, as those appear in the works of [12,13]. The discretization in space is based on the *modal version* of spectral/*hp* elements while in time a high-order splitting scheme is employed [14]. Monotonicity is maintained using a diffusion convolution kernel that controls the high-order modes, the so-called spectral vanishing viscosity (SVV) method.

SVV was first introduced by Tadmor in [15] in the context of constructing *monotonicity-preserving* discretizations to hyperbolic conservation laws. More recently, it has been employed successfully in formulating alternative large-eddy simulation (LES) approaches [16]. Also, in [17], the Legendre spectral vanishing method was shown to effectively control the Gibbs phenomenon, while in [18], the SVV approach was employed in two-dimensional (2D) simulation of waves in stratified atmosphere. The SVV approach guarantees an essentially non-oscillatory behavior although some small oscillations of *bounded amplitude* may be present in the solution. This theory is based on three key components:

1. A vanishing viscosity amplitude which decreases with the mode number.
2. A viscosity-free spectrum for the lower most energetic modes.
3. An appropriate viscosity kernel for the high wavenumbers.

This effective regularization is determined by parameters whose range is given directly by the *non-linear* theory for advection-dominated systems. More recent work has extended the method to superviscosity formulations, first by Tadmor [19] and later by Ma [20,21], in order to extend the range of the *viscosity-free* spectrum.

In this paper, we demonstrate the use and effectiveness of this technique using both analytic solutions as well as standard benchmark problems in two and three dimensions. We also present new results for unsteady flow past a three-dimensional ellipsoid at Reynolds number up to  $Re = 1075$ .

## 2. Mathematical formulation

### 2.1. Governing equations for the FENE-P model

Incompressible viscoelastic flows for diluted polymer solutions can be modeled by a set of three equations: the equation for momentum conservation, the constitutive relationship describing the evolution of the non-Newtonian part of the stress tensor and, finally, the divergence-free condition for the velocity components. In this work we will specifically examine the FENE-P model. This model is based on the assumption of a dumbbell shape for the polymer chains, and is further described by a function due to Peterlin that incorporates the maximum value allowed for the extension of the polymer chains. The non-dimensional momentum conservation equation takes the form:

$$\frac{\partial \mathbf{u}}{\partial t} + \mathbf{u} \cdot \nabla \mathbf{u} = -\nabla p + \frac{1}{Re} [\beta \nabla^2 \mathbf{u} + (1 - \beta) \nabla \cdot \mathbf{s}] + \mathbf{F}, \quad (1)$$

where  $\mathbf{u}$  denotes the velocity vector,  $\mathbf{s}$  denotes the stress contribution due to the viscoelastic properties of the fluid, and  $\beta$  denotes the ratio of the viscosities  $\eta_s/(\eta_s + \eta_p)$ . Here  $\eta_s$  is the viscosity of the solvent and  $\eta_p$  the viscosity of the polymer. Clearly, when  $\beta = 1$  this reduces to the Newtonian case. The Reynolds number in the above equation is defined as  $Re = \rho UL/(\eta_s + \eta_p)$ , with  $U$ ,  $L$  and  $\rho$  denoting characteristic values of the velocity, length and density of the flow, respectively. The FENE-P model is based on a non-linear relation between the *stress* tensor  $\mathbf{s}$  and the *conformation* tensor  $\mathbf{c}$ . The stress tensor  $\mathbf{s}$  is defined through  $\mathbf{c}$  by:

$$\mathbf{s} = \frac{f(r)\mathbf{c} - \mathbf{I}}{We}. \quad (2)$$

Here  $We$  denotes the Weissenberg number defined as  $We = \lambda\kappa$ , where  $\kappa$  is a typical shear rate of the flow and  $\lambda$  a characteristic time constant related to the phenomenon of stress relaxation, typical of viscoelastic fluids. We can further define the Deborah number  $De = \lambda/T$ , where the unit of time  $T$  should be a typical time scale of the flow. However, we will only be using the Weissenberg number definition throughout. In the above equation  $f(r)$  can be identified as the *Peterlin function*:

$$f(r) = \frac{L^2 - R^2}{L^2 - r^2}, \quad (3)$$

where  $r^2 = \text{trace}(\mathbf{c})$  and the small correction  $R$  is usually set to zero, by redefining  $We$  and  $L$ . However, for consistency with other definitions, e.g. [10,12], here we will require  $R = \sqrt{3}$  (for three dimensions) and  $R = \sqrt{2}$  (for two dimensions) since this proves to be convenient when we derive the conformation tensor analytic solution in the convergence studies. In the above relation,  $L$  is the maximum extensibility of the polymer chain. The conformation tensor has been non-dimensionalized by  $k_b T_0/H$ , where  $k_b$  is the Boltzmann constant,  $T_0$  the absolute temperature and  $H$  the spring constant of the FENE-P dumbbell. The evolution equation for the conformation tensor  $\mathbf{c}$  is given by:

$$\frac{\partial \mathbf{c}}{\partial t} + \mathbf{u} \cdot \nabla \mathbf{c} - [\mathbf{c} \cdot (\nabla \mathbf{u}) + (\nabla \mathbf{u})^T \cdot \mathbf{c}] = -\frac{f(r)\mathbf{c} - \mathbf{I}}{We}, \quad (4)$$

where T denotes transposition. The left-hand side of (4) is known as the *upper convected derivative*. The boundary conditions for the conformation tensor will be specifically discussed in the problems of Sections 3–5.

## 2.2. Discretization

For the temporal discretization of the Navier–Stokes equations we use a time-splitting stiffly-stable scheme. Stiffly-stable type schemes enhance stability through backwards differentiation. The implemented scheme has three different steps and it is an extension of the high-order splitting scheme proposed in [22].

### 1. Non-linear step:

$$\hat{\mathbf{u}} = \sum_{q=0}^{J_u-1} \alpha_q \mathbf{u}^{n-q} + \Delta t \sum_{q=0}^{J_u-1} \beta_q \left[ -(\mathbf{u}^{n-q} \cdot \nabla) \mathbf{u}^{n-q} + \frac{(1-\beta)}{Re} \nabla \cdot \mathbf{s}^{n-q} + F^{n-q} \right], \quad (5)$$

where  $\mathbf{s}$  is the contribution from the polymer computed from:

$$\mathbf{s}^n = \frac{f(r) \mathbf{c}^n - \mathbf{I}}{We}. \quad (6)$$

The evolution equation of the conformation tensor is discretized using the following scheme:

$$\hat{\mathbf{c}} = \mathbf{c}^n + \Delta t \sum_{q=0}^{J_c-1} \xi_q \left[ \mathbf{c}^{n-q} \cdot \nabla \mathbf{u}^{n-q} + (\nabla \mathbf{u}^{n-q})^T \cdot \mathbf{c}^{n-q} - (\mathbf{u}^{n-q} \cdot \nabla) \mathbf{c}^{n-q} - \frac{[f(r) \mathbf{c}]^{n-q} - \mathbf{I}}{We} \right]. \quad (7)$$

For stabilization a convolution kernel that introduces the proper amount of diffusion is then employed (see next section) as follows:

$$\epsilon \nabla \cdot (\mathcal{Q}_N * \nabla \mathbf{c}^{n+1}) - \frac{1}{\Delta t} \mathbf{c}^{n+1} = -\frac{\hat{\mathbf{c}}}{\Delta t}, \quad (8)$$

where  $\mathcal{Q}_N$  is a smooth kernel that controls which modes (wavenumbers) are affected.

The implemented boundary condition for the two-dimensional case are  $\partial \mathbf{c} / \partial n^{n+1}|_{\Gamma} = 0$  and  $\mathbf{c}^{n+1}|_{\Gamma} = \hat{\mathbf{c}}|_{\Gamma}$ . In the three-dimensional case we only implemented the latter. We have systematically studied the effect of both of the above boundary conditions, showing that accuracy is not affected by them. From the numerical experiments that we performed, the Neumann boundary condition seems to enhance stability. Also, our benchmark results do not show any appreciable differences as will be shown in Sections 3 and 4.

In the above notation  $J_u \in \{1, 2, 3\}$  is the extrapolation order for the velocity field,  $J_c = 2$  the integration order of the conformation tensor,  $n$  the current time step,  $\alpha_q, \beta_q$  are coefficients associated with the stiffly-stable scheme [22] as shown in Table 1,  $\xi_q$  coefficients associated with the Adams–Bashforth scheme, T denotes matrix transposition,  $N$  denotes  $N$ th polynomial order,  $(*)$  denotes the convolution operator, and finally  $|_{\Gamma}$  denotes value evaluation at the boundary.

### 2. Pressure step:

$$\nabla^2 p^{n+1} = \nabla \cdot \left( \frac{\hat{\mathbf{u}}}{\Delta t} \right), \quad (9)$$

with the boundary condition

$$-\frac{\partial p^{n+1}}{\partial n} = \mathbf{n} \cdot \left[ -\hat{\mathbf{u}} + \frac{\beta}{Re} \sum_{q=0}^{J_p-1} \beta_q \nabla \times (\nabla \times \mathbf{u}^{n-q}) \right]. \quad (10)$$

Table 1  
Coefficients  $\alpha_q, \beta_q, \gamma_0$  associated with the stiffly-stable scheme

Coefficient	First order	Second order	Third order
$\gamma_0$	1	3/2	11/6
$\alpha_0$	1	2	3
$\alpha_1$	0	-1/2	-3/2
$\alpha_2$	0	0	1/3
$\beta_0$	1	2	3
$\beta_1$	0	-1	-3
$\beta_2$	0	0	1

3. Viscous step:

$$\left[ \nabla^2 - \frac{\gamma_0 Re}{\beta \Delta t} \right] \mathbf{u}^{n+1} = -\frac{\gamma_0 Re}{\beta \Delta t} \hat{\mathbf{u}} + \frac{\gamma_0 Re}{\beta} \nabla p^{n+1}. \tag{11}$$

In the above notation  $J_p \in \{1, 2, 3\}$  is the extrapolation order for the pressure. The overall temporal accuracy of the scheme is  $\mathcal{O}(\Delta t^2)$  and it is dictated by  $J_c = 2$ ; it can be readily extended to third-order in time similar to the velocity solver in the Newtonian case [22].

For *spatial discretization* we have adopted the spectral/*hp* element method, see [14]. It employs standard unstructured and hybrid grids unlike previous approaches that require special structured grids. This new version of spectral element uses a hierarchical basis based on Jacobi polynomials with mixed weights that accommodate accurate numerical quadrature and flexibility in discretization by employing *polymorphic subdomains*. The degenerate case corresponds to a linear finite element discretization with the vertices corresponding to linear modes. Each element consists of  $N$  modes per direction but no gridding within the element is required as all computations are done in modal space. Specifically, each element is separated into linear vertex modes, edge modes, face modes and interior or bubble modes.

For a smooth solution, the error in a Galerkin projection of a smooth function is converging exponentially fast to zero by simply increasing the number of modes per element/subdomain. This allows for selective refinement and sharp a priori error estimates in the numerical solution without the overhead cost associated with re-generation of a three-dimensional mesh. Another distinction with other versions of the *hp* finite element methods that employ monomials is that very high-order is readily employed (e.g.  $N = 32$ ) and that the multi-dimensional basis is a tensorial product in the transformed domain [14]. This, in turn, leads to good efficiency in simulations with high-order  $N$ .

The new method has been implemented in the serial and parallel versions of the computer code named *N $\epsilon$ KTar* [23].

2.3. The spectrally vanishing viscosity (SVV) method

Tadmor [15] first introduced the concept of spectral vanishing viscosity for hyperbolic conservation laws. Specifically, he used the inviscid Burgers’ equation:

$$\frac{\partial}{\partial t} u(x, t) + \frac{\partial}{\partial x} \left( \frac{u^2(x, t)}{2} \right) = 0, \tag{12}$$

subject to given initial and boundary conditions. The distinct feature of solutions to this problem is that spontaneous jump discontinuities (shock waves) may be developed, and hence a class of weak solutions can be admitted. Within this class, there are many possible solutions, and in order to single out the physically relevant one an additional entropy condition is applied, of the form:

$$\frac{\partial}{\partial t} \left( \frac{u^2(x, t)}{2} \right) + \frac{\partial}{\partial x} \left( \frac{u^3(x, t)}{3} \right) \leq 0. \quad (13)$$

In the context of viscoelastic flows the objective is to obtain a unique stable solution of the conformation stress equation. Tadmor [15] introduced the spectral vanishing viscosity method, which adds a small amount of *mode-dependent* dissipation that satisfies the entropy condition, yet retains spectral accuracy. It is based on viscosity solutions of non-linear Hamilton–Jacobi equations, which have been studied systematically in [24]. Specifically, the viscosity solution for the Burgers’ equation has the form:

$$\frac{\partial}{\partial t} u(x, t) + \frac{\partial}{\partial x} \left( \frac{u^2(x, t)}{2} \right) = \epsilon \frac{\partial}{\partial x} \left[ Q_\epsilon \frac{\partial u}{\partial x} \right], \quad (14)$$

where  $\epsilon (\rightarrow 0)$  is a viscosity amplitude and  $Q_\epsilon$  a viscosity kernel. Convergence may then be established by compactness estimates combined with entropy dissipation arguments [15]. To respect spectral accuracy, the SVV method makes use of viscous regularization, and Eq. (14) may be rewritten in discrete form (retaining  $N$  modes):

$$\frac{\partial}{\partial t} u_N(x, t) + \frac{\partial}{\partial x} \left[ \mathcal{P}_N \left( \frac{u^2(x, t)}{2} \right) \right] = \epsilon \frac{\partial}{\partial x} \left[ Q_N * \frac{\partial u_N}{\partial x} \right], \quad (15)$$

where the star (\*) denotes convolution and  $\mathcal{P}_N$  is a projection operator.  $Q_N$  is a viscosity kernel, which is only activated for high wavenumbers. In Fourier space, this kind of spectral viscosity can be efficiently implemented as multiplication of the Fourier coefficients of  $u_N$  with the Fourier coefficients of the kernel  $Q_N$ , i.e.

$$\epsilon \frac{\partial}{\partial x} \left[ Q_N * \frac{\partial u_N}{\partial x} \right] = -\epsilon \sum_{M \leq |k| \leq N} k^2 \hat{Q}_k(t) \hat{u}_k(t) e^{ikx},$$

where  $k$  is the wavenumber,  $N$  the number of Fourier modes, and  $M$  the wavenumber above which the spectral vanishing viscosity is activated.

Originally, Tadmor [15] used

$$\hat{Q}_k = \begin{cases} 0, & |k| \leq M \\ 1, & |k| > M, \end{cases} \quad (16)$$

with  $\epsilon M \sim 0.25$  based on the consideration of minimizing the total-variation of the numerical solution. In subsequent work, however, a smooth kernel was used, since it was found that the  $C^\infty$  smoothness of  $\hat{Q}_k$  improves the resolution of the SVV method. For Legendre pseudo-spectral methods, Maday et al. [25] used  $\epsilon \approx N^{-1}$ , activated for modes  $k > M \approx 5\sqrt{N}$ , with

$$\hat{Q}_k = e^{-(k-N)^2/(k-M)^2}, \quad k > M. \quad (17)$$

In order to see the difference between the convolution operator on the right-hand side in Eq. (15) and the usual viscosity regularization, following Tadmor [26], we expand as:

$$\epsilon \frac{\partial}{\partial x} \left[ Q_N * \frac{\partial u_N}{\partial x} \right] = \epsilon \frac{\partial^2 u_N}{\partial x^2} - \epsilon \frac{\partial}{\partial x} \left[ R_N(x, t) * \frac{\partial u_N}{\partial x} \right], \quad (18)$$

where

$$R_N(x, t) \equiv \sum_{k=-N}^N \hat{R}_k(t) e^{ikx}; \quad \hat{R}_k(t) \equiv \begin{cases} 1 - \hat{Q}_k(t), & |k| \geq M \\ 1, & |k| < M \end{cases}. \quad (19)$$

The extra term appearing in addition to the first standard viscosity term makes this method different. It measures the distance between the spectral (vanishing) viscosity and the standard viscosity. This term is bounded in the  $L_2$  norm similarly to the spectral projection error. In this paper we refer to the viscosity as vanishing as the theory requires that

$$\epsilon \approx \frac{1}{N^\theta \log N}, \quad \theta \leq 1,$$

and thus  $\epsilon \rightarrow 0$  for high wavenumbers.

The basis we use is written in terms of Jacobi polynomials and is decomposed into *vertex* modes, *edge* modes and *interior* modes. This is a semi-orthogonal basis (see [14] for details) but the SVV procedure should be applied to orthogonal modes. To this end, we will transform the semi-orthogonal basis to the orthogonal one as outlined below.

If we examine the weak form of the SVV term  $\epsilon(\partial/\partial x)(Q_\epsilon(\partial u/\partial x))$  only, ignoring boundary terms and the leading coefficient, we have the following basic form of the SVV operator:

$$\left( \frac{\partial v}{\partial x}, Q \frac{\partial u}{\partial x} \right) \quad (20)$$

where  $v$  is a test function taken from the Jacobi polynomials  $\{\phi_k\}$  and  $u = \sum_k \hat{u}_k \phi_k$ . In the derivation below we will assume that all discrete summations are from  $1, \dots, N$ . In the notation above and henceforth  $(\cdot, \cdot)$  denotes the  $L_2$  inner product and it is assumed that the continuous and discrete inner products are interchangeable given sufficient quadrature order.

Now, let  $\mathbf{B}$  be a matrix that transforms the modal coefficients  $\hat{u}$  for the basis functions  $\{\phi_k\}$  to  $\tilde{u}$  in the  $\{\psi_k\}$  space, where  $\{\phi_k\}$  is our  $C^0$  basis used for the Galerkin formulation and  $\{\psi_k\}$  is an *orthonormal* basis that spans the same space as  $\{\phi_k\}$ . Let  $\mathbf{F}$  be a diagonal matrix that acts as a filtering function (the entries of which are given by Eq. (17)). In the notation above we have  $\tilde{u} = \mathbf{B}\hat{u}$ . Our goal is to filter the coefficients  $\tilde{u}$  instead of filtering the coefficients  $\hat{u}$ . Hence, we would like to transform (via the matrix  $\mathbf{B}$ ) to the orthogonal space, filter, and then transform back. This can be accomplished by the operation:

$$\hat{u} = \mathbf{B}^{-1} \mathbf{F} \mathbf{B} \hat{u}. \quad (21)$$

We can now write expression (20) in the discrete form using matrix notation as follows:

$$\mathbf{S}^T \mathbf{B}^{-1} \mathbf{F} \mathbf{B} \mathbf{M}^{-1} \mathbf{S} \hat{u}, \quad (22)$$

where  $S_{ij} = (\phi_i, \partial\phi_j/\partial x)$  and  $M_{ij} = (\phi_i, \phi_j)$ . It can be shown that  $B^{-1} = M^{-1}B^T$ , and hence the discrete form of the SVV operator for the Galerkin method is given by:

$$S^T M^{-1} B^T F B M^{-1} S \hat{u}. \quad (23)$$

Note that the above discrete operator is symmetric, semi-positive definite.

The above formulation was first introduced by Kirby [27] for LES. It has been suggested that the artificial viscosity added usually in the stress equation in physical space is analogous to subgrid viscosity in large-eddy simulations. That is, instabilities typically arise when the small scales are under-resolved and correspondingly solution monotonicity is lost. To this end, it is instructive to compare the spectral vanishing viscosity to the spectral eddy-viscosity introduced by Kraichnan [28] as modified by Lesieur and Metais [29] and Chollet [30]. The latter has the non-dimensional form [30]:

$$\nu(k/N) = K_0^{-3/2} [0.441 + 15.2 \exp(-3.03N/k)], \quad K_0 = 2.1 \quad (24)$$

Comparing the Fourier analog of this eddy-viscosity employed in LES [29] to the viscosity kernel  $Q_k(k, M, N)$  introduced in the SVV method, Fig. 1 shows both viscosity kernels normalized by their maximum value at  $k = N$ . For SVV two different values of the cut-off wavenumber are considered, i.e.

$$M = C\sqrt{N} \quad \text{for } C = 0 \text{ and } 5, \quad (25)$$

and are shown in the plot of Fig. 1. In particular, the solid line can be thought of as a *stability barrier* above which monotonicity and thus stability is not guaranteed. On the other hand, the dash line can be

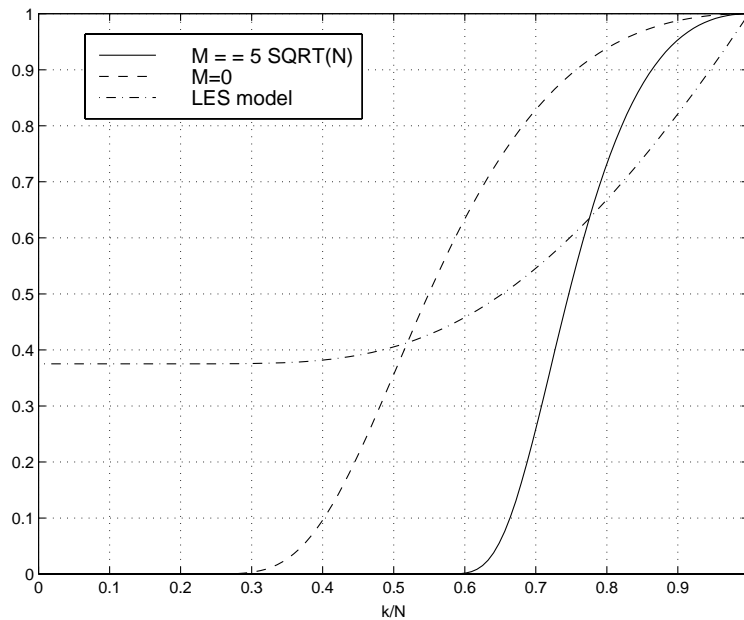


Fig. 1. Normalized viscosity kernels for the spectral vanishing viscosity (dash line  $C = 0$  and solid line  $C = 5$ ) and the Kraichnan/Chollet–Lesieur viscosity (dash–dot line).

thought of as an *accuracy barrier* below which the convergence of the method is affected. This range has been used in most of the numerical experiments so far (see for example [16,18,25]) and is consistent with the theoretical results [15]. In the plot it is shown that, in general, the two forms of viscosity have similar distributions but the SVV form does not affect the first one-third or one-half of the spectrum (viscosity-free portion) and it increases faster than the Kraichnan/Chollet–Lesieur eddy-viscosity in the higher wavenumbers range, e.g. in the second-half of the spectrum.

In the following, we will address the effect of SVV on the convergence rate and the stability of spectral/*hp* element discretization.

### 3. Convergence and SVV parameters

The convergence tests used to show the effect of SVV are based on an analytic solution derived for the conformation tensor in a channel flow. By letting  $R = \sqrt{2}$  for a two-dimensional flow and  $R = \sqrt{3}$  for a three-dimensional flow in Eq. (3), we can simplify the analytic solution for velocity fields of the form  $\mathbf{u} = (U(y), 0, 0)$ . Thus, we can examine the effect of the two different parameters appearing on the SVV formulation (the cut-off mode  $M$  and the value of  $\varepsilon$ ) and the  $L_2$  error of the numerical results when compared to the analytic solution. As stated in [10], the exact solution of the conformation tensor for a three-dimensional problem can be identified as the following (symmetric) matrix:

$$\mathbf{c} = \begin{pmatrix} \frac{1}{F(y)} \left[ 1 + \frac{2We^2}{F^2(y)} \left( \frac{dU}{dy} \right)^2 \right] & \frac{We}{F^2(y)} \left( \frac{dU}{dy} \right) & 0 \\ & \frac{1}{F(y)} & 0 \\ & & \frac{1}{F(y)} \end{pmatrix}, \tag{26}$$

where the following definitions apply:

$$\Omega(y) = \frac{\sqrt{2}We}{L} \frac{dU}{dy}, \tag{27}$$

$$F(y) = \frac{\sqrt{3}\Omega(y)}{2\sinh(\phi/3)}, \tag{28}$$

$$\phi = \sinh^{-1} \left( \frac{3\sqrt{3}\Omega}{2} \right). \tag{29}$$

For the two-dimensional case we reduce the value of  $R$  from  $\sqrt{3}$  to  $\sqrt{2}$  and consequently only the upper left  $2 \times 2$  block appears for the exact expression.

Based on the above analytic expression, we conclude that the exact relation for the conformation tensor subject to the above restrictions is dependent only on the velocity gradient in the  $y$ -direction. Fabricating

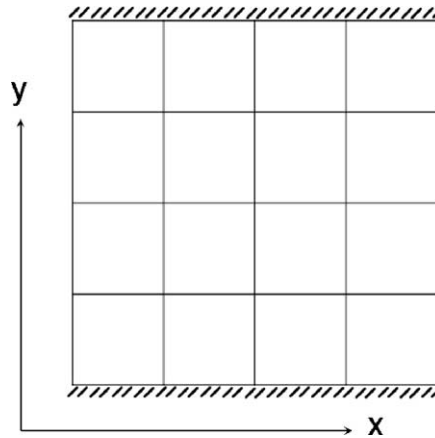


Fig. 2. The 16-element mesh employed for the convergence tests in two dimensions. A similar  $4 \times 4 \times 4$  mesh was used for the three-dimensional convergence tests. The channel has a length of 2 in all directions.

a non-trivial solution for the flow field for  $y \in [-1, 1]$  other than the parabola  $U(y) = 1 - y^2$  requires the introduction of a more complicated expression for the driving force  $\mathbf{F}$  in Eq. (1). It can be shown that if

$$F_x = \sqrt{\frac{2}{3}} \frac{L}{Re We} [\beta \cosh(3y) + (1 - \beta) \cosh(y)] \quad (30)$$

the corresponding expression for the velocity has the simple but non-trivial form:

$$U(y) = \frac{\sqrt{2}}{9\sqrt{3}} \frac{L}{We} [\cosh(3) - \cosh(3y)]; \quad y \in [-1, 1]. \quad (31)$$

Both a two- and three-dimensional test case (the  $z$ -axis is normal to the paper in Fig. 2) have been investigated to evaluate the convergence rate of the method. For brevity, we only present the three-dimensional results below.

The mesh we employ for the three-dimensional tests consists of  $4 \times 4 \times 4$  elements and the domain is similar to the one shown in Fig. 2 with all three sides of length 2. We have set  $Re = 8$  and  $We = 25$  and considered two values of the coupling parameter  $\beta$ . In Fig. 3 we plot the  $L_2$  error in the velocity and the conformation tensor (all components); we see that the solution error converges exponentially to zero for both fields. Solutions are obtained for  $N = 5, 7$  and  $11$  with corresponding SVV parameters  $(\varepsilon, M) = (0.05, 2); (0.02, 4); (0.01, 6)$ . We see that despite the use of artificial viscosity the formal (exponential) accuracy of the discretization is maintained. This is true irrespective of the size of the coupling parameter  $\beta$  although, as expected, the greater the value of  $(1 - \beta)$  the larger the error value is.

Next we examine how sensitive the numerical solution is with respect to the choice of the SVV parameters; we fix the spectral order to  $N = 7$ . In Fig. 4 we plot the  $L_2$  error of the conformation tensor (all components) versus the SVV amplitude  $\varepsilon$  (left) and cut-off wavenumber  $M$ . With respect to the latter, we see indeed that for larger values we run into a stability barrier whereas for low values the accuracy degrades; such trends are valid for different values of the SVV amplitude as shown in Fig. 4 (right). The stability and accuracy trends with respect to viscosity amplitude  $\varepsilon$  are also in agreement with Tadmor's theory although here the *optimum* value of  $\varepsilon$  cannot be predicted precisely by the theory.

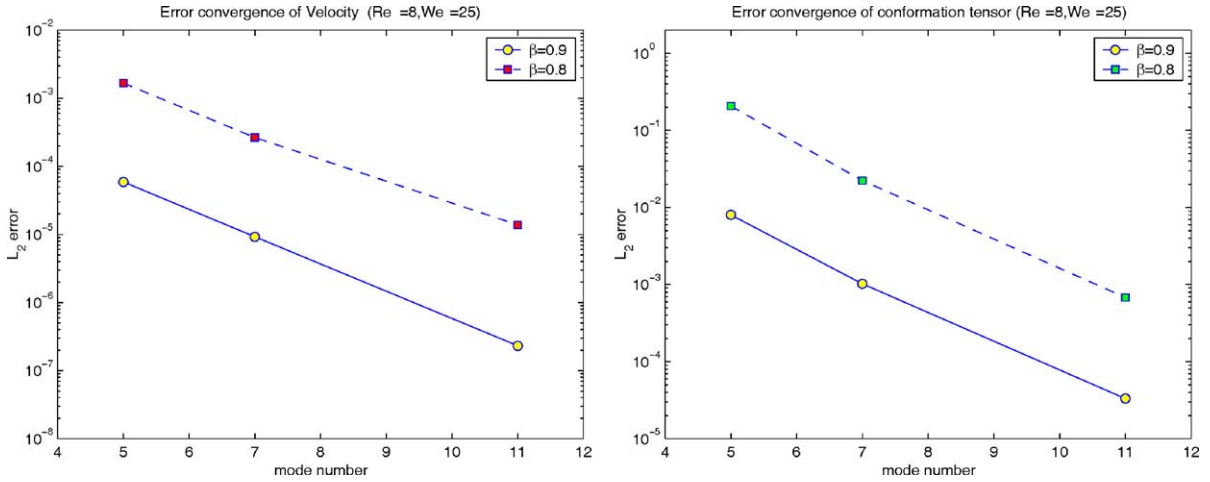


Fig. 3. Three-dimensional case: convergence rate in velocity (left) and conformation tensor (right).

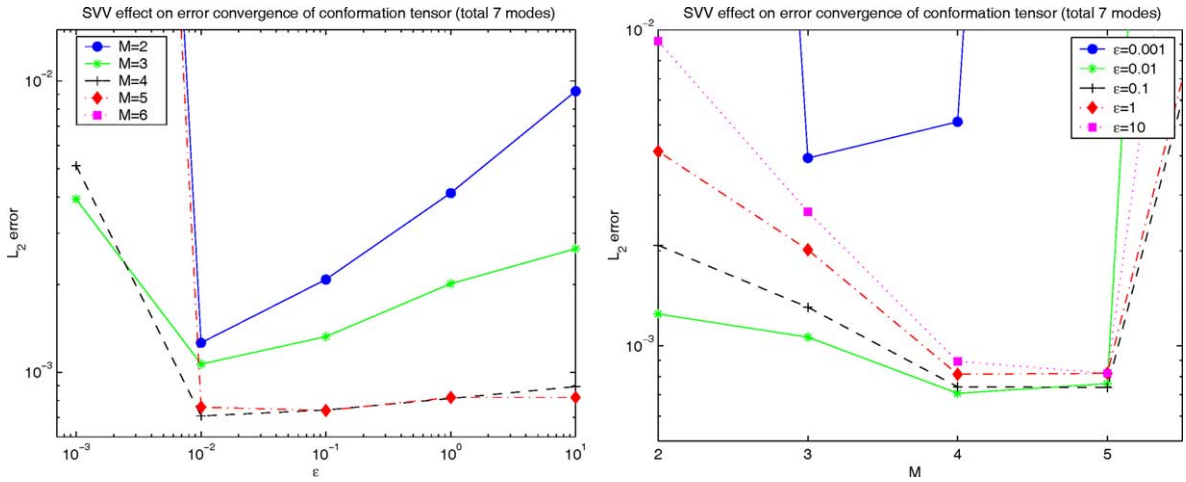


Fig. 4. Three-dimensional case: effects of SVV amplitude (left) and cut-off wavenumber (right).

As a final remark on the selection of the two different boundary conditions  $\partial c / \partial n^{n+1}|_{\Gamma} = 0$  and  $c^{n+1}|_{\Gamma} = \hat{c}|_{\Gamma}$ , we show in Fig. 5 that accuracy is not significantly affected by favoring one or the other. The plot shows the *difference* in the  $L_2$  error between the two, normalized by the  $L_2$  error of the Dirichlet boundary condition.

#### 4. Benchmark problems—Stokes flow

To demonstrate the stability and accuracy of the method, we will compare with some of the most commonly published results on specific benchmark problems, for both two- and three-dimensional simulations.

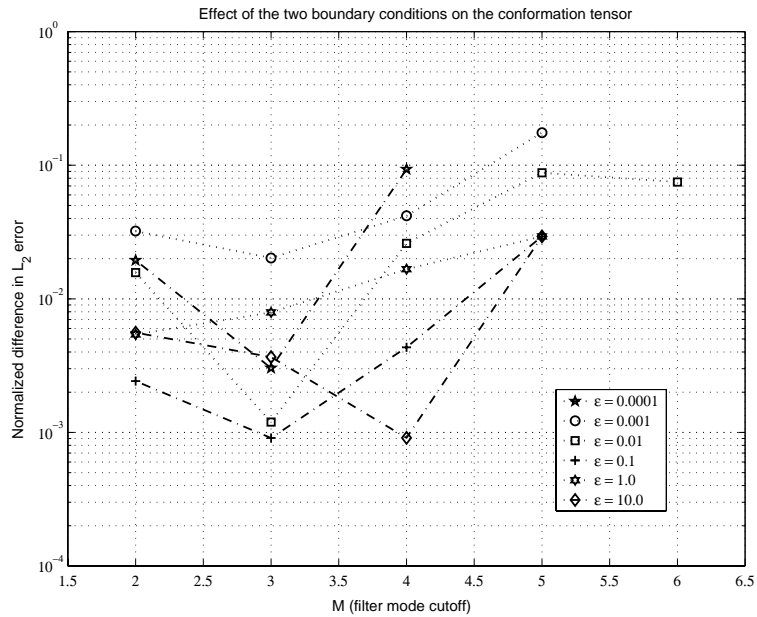


Fig. 5. Effect of the two different boundary conditions  $\partial c/\partial n^{n+1}|_T = 0$  and  $c^{n+1}|_T = \hat{c}|_T$  on the  $L_2$  error. Results shown are from the two-dimensional (analytical) case.

#### 4.1. Cylinder in a channel

The robustness of the scheme will first be demonstrated in the well-examined flow past a two-dimensional cylinder in a symmetric channel. Here, we do not make use of the symmetry, and thus we include the entire domain, unlike past studies. The computational mesh employs 176 quadrilateral elements as shown in Fig. 6.

The setup of the problem is as follows. The length of the channel is 40 non-dimensional units long ( $x \in [-20, 20]$ ), the channel half-width  $H$  is 2 units long ( $y \in [-2, 2]$ ), the radius of the cylinder  $R$  is 1

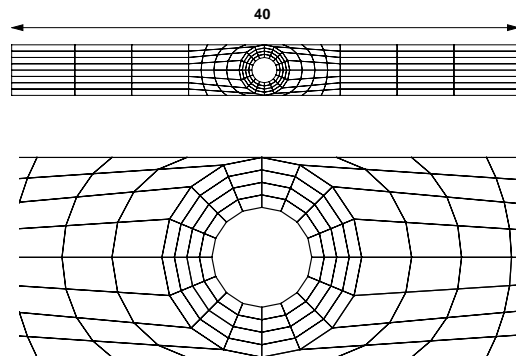


Fig. 6. The two-dimensional mesh used for the benchmark problem. The curved sides are represented isoparametrically with a high-order expansion. Here, faces are plotted as straight lines.

Table 2

Time step  $\Delta t$  with SVV parameter  $\varepsilon = 0.001$  and  $M = 2$  for each successful case

$We$	$N = 5$	$N = 6$	$N = 7$	$N = 8$	$N = 9$
0.505	1E-4	1E-4	1E-4	3E-5	1E-5
0.608	1E-4	1E-4	1E-4	3E-5	1E-5
0.712	1E-4	1E-4	5E-5	3E-5	1E-5
0.818	1E-4	5E-5	1E-5	1E-5	1E-5

 $N$  denotes the spectral order per direction.

unit long ( $R = 1$ ) and consequently the aspect ratio  $\Lambda = R/H = 1/2$ . Parabolic inflow of the form

$$u_x(y) = \frac{3}{2}U \left( 1 - \left( \frac{y}{H} \right)^2 \right),$$

$$u_y = 0,$$

is imposed along  $y \in [-2, 2]$  at  $x = -20$ , thus the mean value  $U = 1$ . The outflow boundary condition at  $x = 20$  is treated with Neumann boundary condition set to zero. The boundary conditions for the conformation tensor in the entrance of the channel are Dirichlet and are set to be the analytic values corresponding to  $\beta = 1$  as dictated by Eq. (26). We also define the Weissenberg number for this flow to be  $We = U\lambda/R$ . Choosing the SVV parameters  $(\varepsilon, M) = (0.001, 2)$  throughout, the time step  $\Delta t$  is adjusted as shown in Table 2. The evolution Eq. (4) for the conformation tensor is solved in physical space explicitly, using the second-order Adams–Bashforth scheme. The additional SVV part of the equation is solved implicitly in modal space.

The computations are considered steady-state once the stopping criterion

$$\frac{\|\mathbf{u}^{n+1} - \mathbf{u}^n\|_\infty}{\Delta t} < 10^{-3}$$

is met. The simulation parameters<sup>1</sup> chosen for this benchmark problem are  $\beta = 0.59$ ,  $L = \sqrt{20}$ .

Letting  $\tau = (1 - \beta)s$ , we will focus on the *axial normal stress*  $T_{xx} = \tau_{1,1}$  profiles on the rim of the cylinder, the wake, and the stagnation points. Comparisons of these values were done with Chauvière's [13,31] parameters, namely Weissenberg numbers equal to 0.505, 0.608, 0.712 and 0.818. Fig. 7 shows the profiles of the axial normal stress  $T_{xx}$  for a given polynomial order along the  $x$ -direction as the Weissenberg number varies.  $x \in [-1, 1]$  is the region between the two stagnation points. Observing the axial normal stress at the wake and at  $x = 0$ , we see that  $T_{xx}$  has higher values in the wake region as Weissenberg numbers get higher, but inversely for the highest point on the cylinder  $x = 0$ .

Fig. 8 demonstrates the resolution studies made from the aspect of  $p$ -refinement for a given Weissenberg number. The agreement among the five different polynomial orders is clear. Of significance is also the drag coefficient  $F^*$  on the cylinder normalized as:

$$F^* = \frac{F}{4\pi\eta U} \tag{32}$$

<sup>1</sup> Consistency with [13,31] requires in the two-dimensional case a small normalization factor for the stress tensor  $\mathbf{s} = \alpha(L)((f(r)\mathbf{e} - \mathbf{I})/We)$ , where  $\alpha(L) = ((L^2 + 2)/L^2) = 1.1$ .

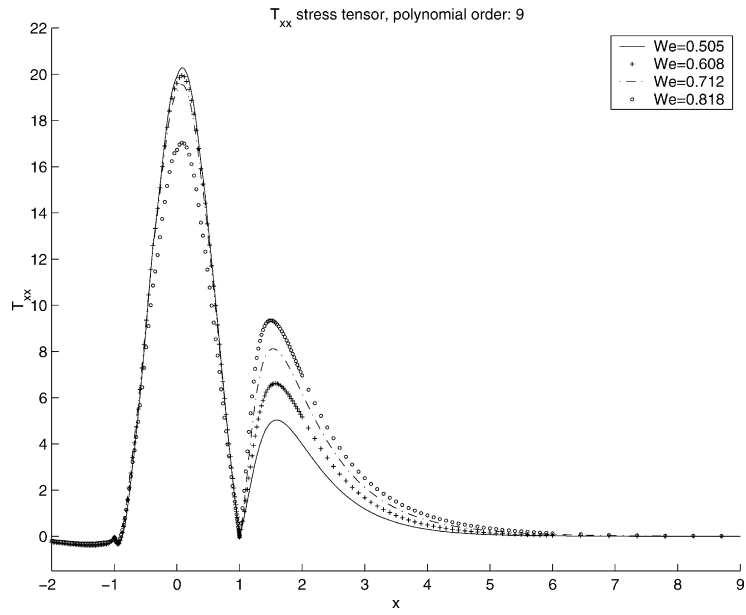


Fig. 7.  $T_{xx}$  stress tensor, polynomial order  $N = 9$ .

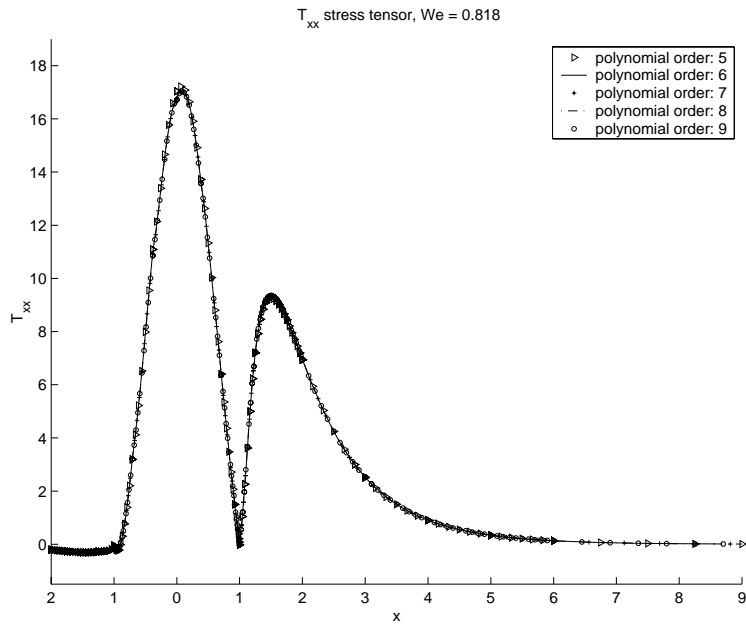


Fig. 8. Effects of  $p$ -refinement:  $T_{xx}$  stress tensor, Weissenberg number  $We = 0.818$ .

Table 3

Drag coefficient  $F^*$  for macroscopic simulations with SVV (upper middle) and drag coefficient  $F^*$  by Chauvière [13] (lower middle)

$We$	$N = 5$	$N = 6$	$N = 7$	$N = 8$	$N = 9$
No SVV					
0.505	8.992	8.998	8.999	9.002	9.006
SVV					
0.505	8.998	9.001	9.002	9.003	9.007
0.608	8.844	8.848	8.850	8.852	8.856
0.712	8.728	8.733	8.738	8.739	8.740
0.818	8.639	8.635	8.652	8.653	8.652
Chauvière [13]					
0.505	9.090	9.093	9.081	9.077	9.076
0.608	8.967	8.979	8.964	8.958	8.957
0.712	8.886	8.906	8.891	–	–
0.818	8.838	–	–	–	–
% difference					
0.505	1.0138	1.0136	0.8655	0.8122	0.7553
0.608	1.3711	1.4579	1.2739	1.1813	1.1303
0.712	1.7782	1.9405	1.7197	–	–
0.818	2.2529	–	–	–	–

Empty boxes correspond to divergent runs. It has to be noted here that the corresponding mesoscopic simulations done in [13] did converge. We also present the drag coefficient for  $We = 0.505$  without applying any SVV filtering (upper). The percentage of difference between Chauvière's values and the SVV values is shown here too (lower).

where  $\eta = \eta_s + \eta_p$  is the total viscosity, and as stated earlier  $U = 1$ . Table 3 demonstrates the robustness of the SVV filtering, as none of the values are diverging to infinity, compared to other methods for macroscopic simulations.

Table 3 also shows the percentage of disagreement between Chauvière [13,31] and the SVV-calculated values. Naturally, increasing the Weissenberg number increases the disagreement. It has to be noted that in this disagreement the effect of the SVV is secondary. To this end, we performed a series of simulations for  $We = 0.505$  (the drag coefficients shown in Table 3) without applying any SVV filtering. The results support the above conclusion. Comparison was also made on the effect of SVV on the  $T_{xx}$  profiles. To this end, results from the standard and modified SUPG method ([13,31], private communications) and the SVV were compared to verify the accuracy and stability of the method. Fig. 9 shows a good agreement for  $We = 0.608$ .

In Fig. 10 we plot the  $T_{xx}$  contours for the Weissenberg number of 0.712 and  $N = 8$  close to the cylinder. Good agreement is established between the two results.

Fig. 11 shows the  $T_{xx}$  profiles for higher Weissenberg numbers, ranging from  $We = 0.88$  up to 2.00. Our simulations appear to be highly stable in this range. No attempt was made to reach higher Weissenberg numbers than  $We = 2.00$ . The qualitative trends agree in these cases as well, i.e. the axial normal stress is higher at the wake of the cylinder for higher Weissenberg numbers but inversely for  $x = 0$ . Fig. 12 also shows the drag coefficient variation for  $N = 6$  with respect to the Weissenberg number.

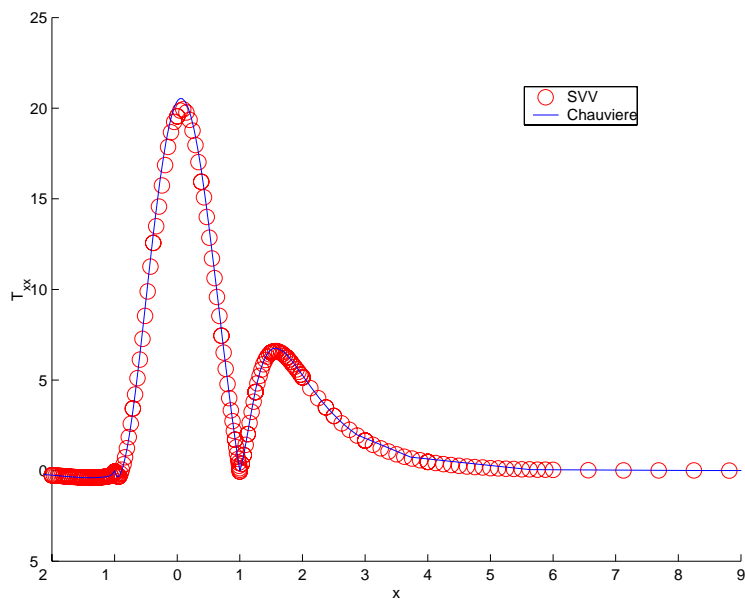


Fig. 9. Comparison of  $T_{xx}$  profiles at  $We = 0.608$  and polynomial order  $p = 8$ .

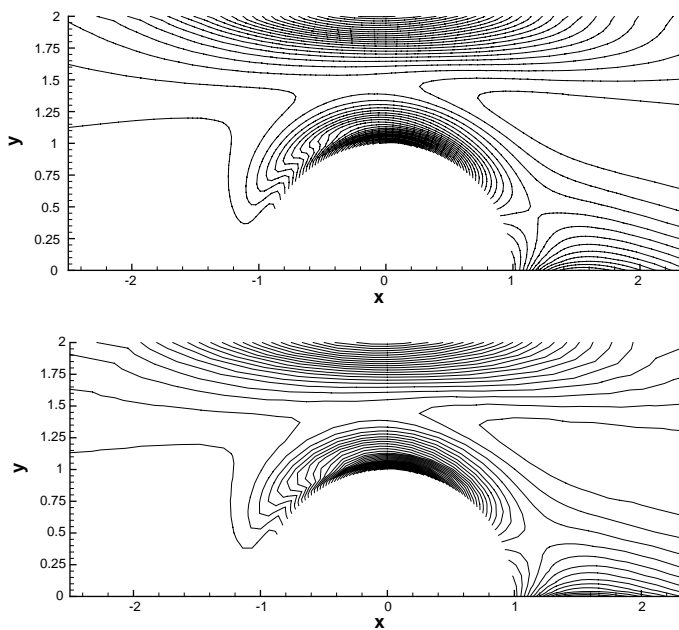


Fig. 10.  $T_{xx}$  contours for  $We = 0.712$  and polynomial order  $N = 8$ . We compare the SVV method (upper) and Chauvière's results [13] (lower).

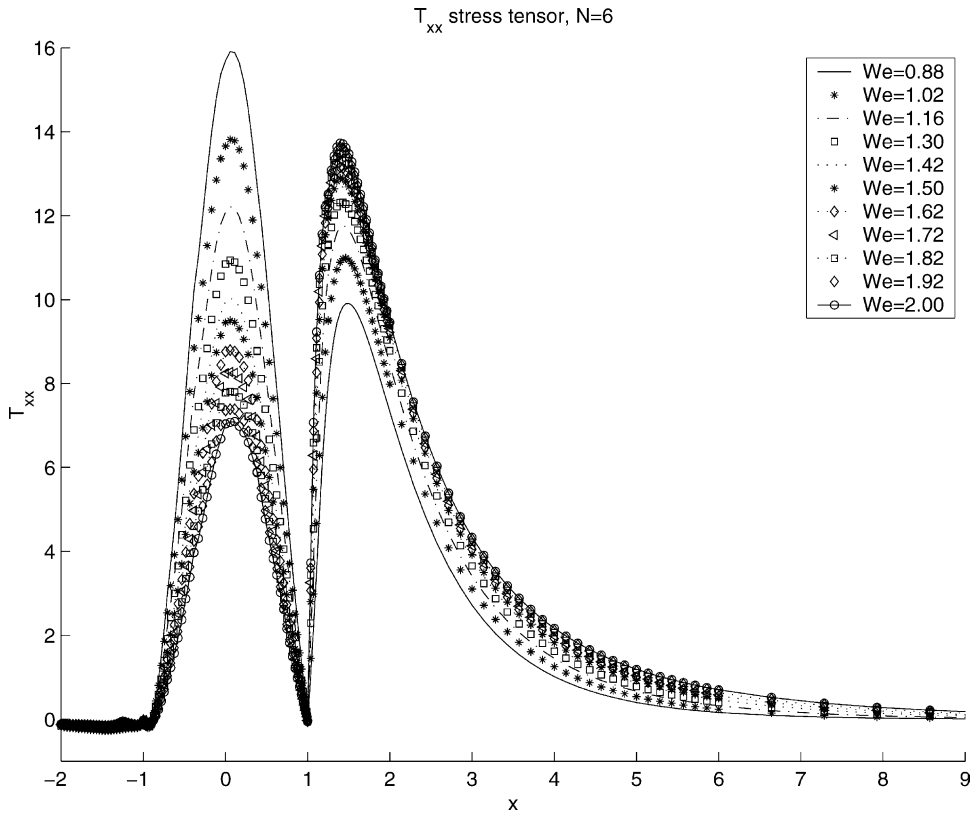


Fig. 11.  $T_{xx}$  profiles for Weissenberg numbers up to 2.0.

Finally, comparing again the effect of the two different boundary conditions  $\partial c / \partial n^{n+1}|_r = 0$  and  $c^{n+1}|_r = \hat{c}|_r$ , Fig. 13 shows no appreciable differences in the axial normal stress profiles for  $We = 0.505$ , verifying the convergence remarks of Section 3.

#### 4.2. Falling sphere in a tube

Next we consider Stokes flow past a sphere in a long tube, a standard benchmark test (adopted in the Fifth Workshop on Numerical Methods of Non-Newtonian Flows). The ratio of the tube to the sphere radius is  $R_t/R_s = 2$ , and we vary the Weissenberg number which is defined here as:

$$We = \frac{\lambda V_s}{R_s}$$

where  $V_s$  is the speed of the sphere. The value of maximum extensibility of the polymer chain here is set to  $L = 6$ , the time step is set to  $\Delta t = 5E-3$  and the SVV parameters are  $\varepsilon = 0.001$  and  $M = 2$ . Dirichlet boundary conditions for the conformation tensor (the diagonal entries of the matrix in this case) are imposed at the front end of the tube, as dictated by Eq. (26).

This problem is a severe test for numerical methods due to the steep stress boundary layers formed around the sphere and the stress wake developed. Several solutions have appeared in the literature for

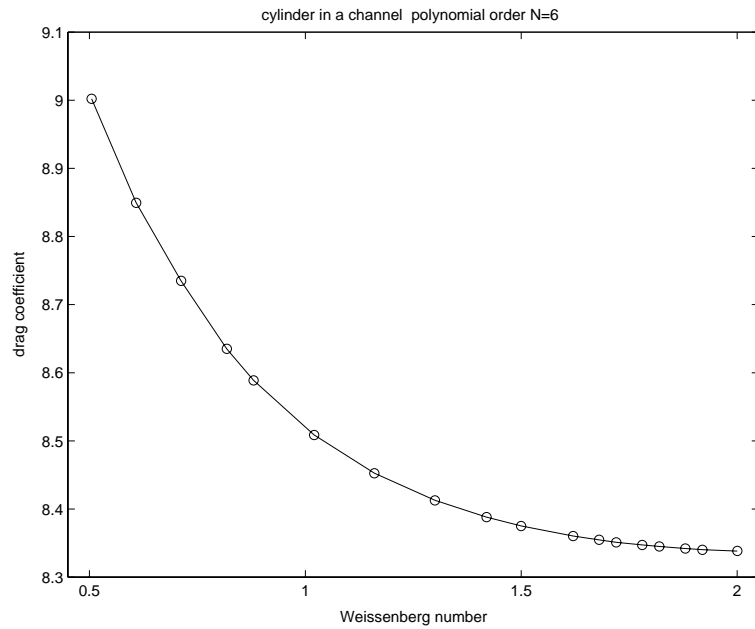


Fig. 12. Drag coefficient for Weissenberg numbers ranging from 0.505 to 2.0.

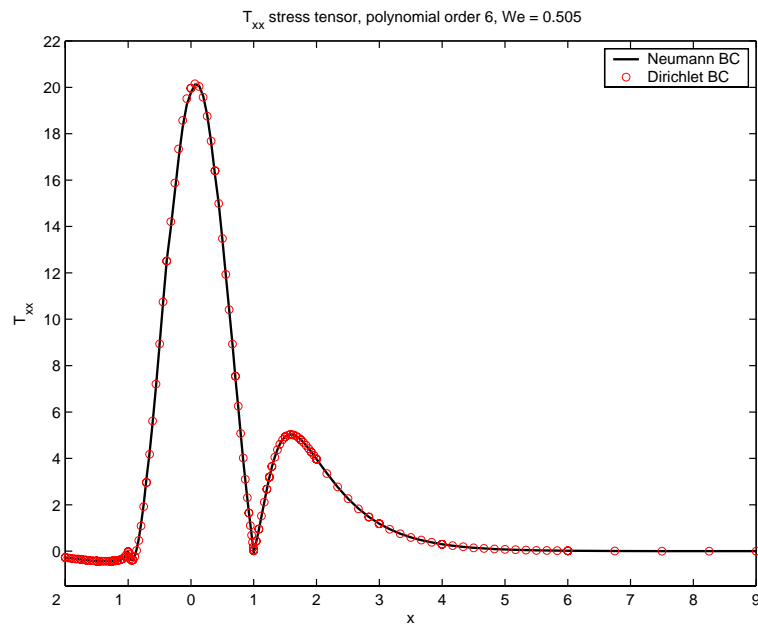


Fig. 13.  $T_{xx}$  profiles for  $We = 0.505$  and polynomial order  $N = 6$ . Here we compare the two different boundary conditions for the conformation tensor.

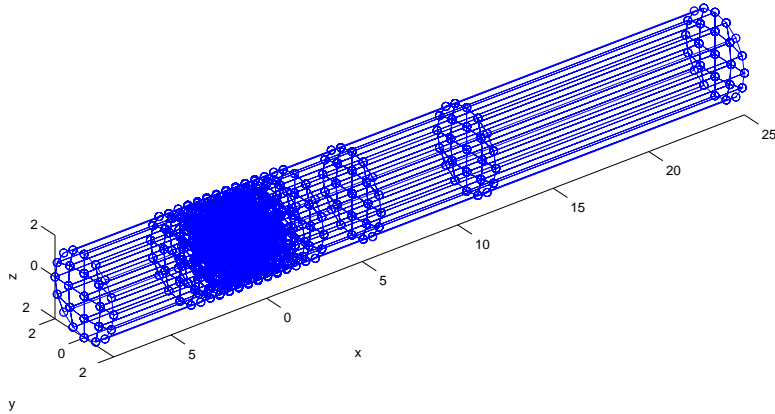


Fig. 14. Three-dimensional mesh for simulating the falling sphere problem. The sphere radius is  $R_s = 1$ .

$We \leq 2.5$  using, e.g.  $p$ -adaptive finite element discretizations [32], discontinuous Galerkin methods [33,34],  $hp$  Galerkin least-square finite element methods [5], and Lagrangian methods [3].

However, unlike previous works where an axi-symmetric formulation is used, here we employ a Cartesian *full three-dimensional* formulation in order to test the new SVV-based formulation. The overall mesh and its details are shown in Figs. 14 and 15; it consists of 608 hexahedra elements. In the simulations we will vary the spectral order  $N$  to test convergence.

The first quantity that we compute is the drag correction factor  $K$  defined by:

$$K = \frac{F}{6\pi\eta_s V_s R_s},$$

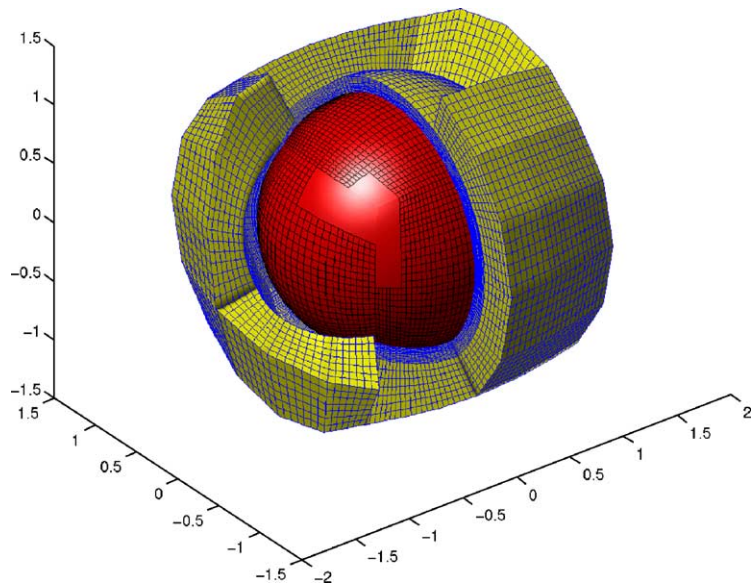


Fig. 15. Detail of the mesh around the sphere for Stokes flow.

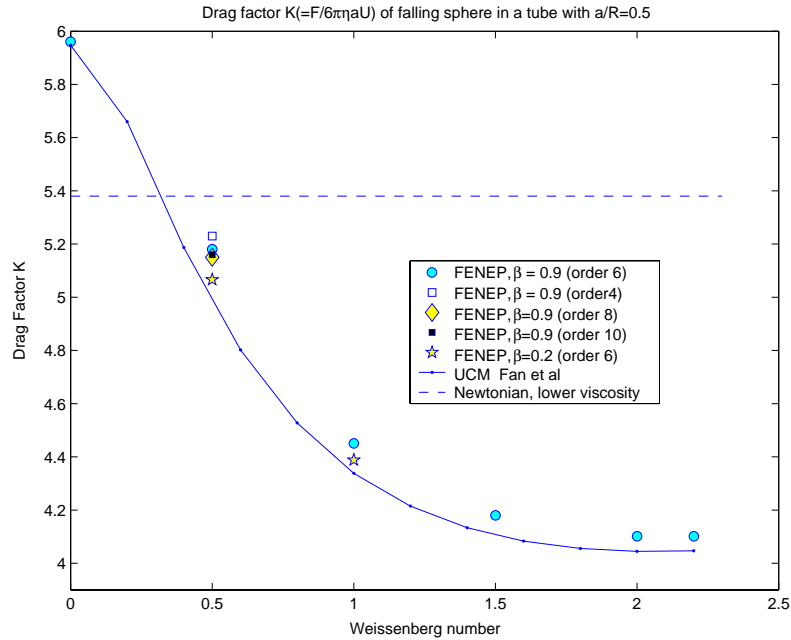


Fig. 16. Drag factor vs. Weissenberg number for sphere in Stokes flow.

where the denominator represents the Stokes drag for a Newtonian fluid in an infinite medium. In Fig. 16 we plot the drag correction factor versus the Weissenberg number and compare with the results of Fan et al. [5]. In that reference an upper-convected Maxwell (UCM) fluid model was used whereas in the current work a FENE-P model is used. In order to investigate the differences between the two results we vary the coupling parameter  $\beta$  in the FENE-P model; we see as  $\beta$  gets smaller the FENE-P solution approaches the UCM solution of Fan et al. [5].

In order to get a first order estimate of the shear-thinning effect, we also performed a simulation by setting  $(1 - \beta)\nabla \cdot s$  to zero in Eq. (1), which is equivalent to a Newtonian simulation with lower viscosity. In Fig. 16, as the Weissenberg number exceeds the value of 0.3, the contributions from the elastic properties of the polymer become apparent in the amount of drag reduction. Of course, more detailed models, as done in [35], have to be employed here to account for the actual effect of shear-thinning.

We have also investigated the effect of resolution by varying the spectral order  $N = 4, 6, 8$  and 10; above  $N = 6$  the solution does not change very much.

We note here that very large values in Weissenberg number have been achieved using, e.g. Lagrangian methods and specially-designed two-dimensional (axi-symmetric) grids, e.g. see [3]. Here, we achieved these solutions on a non-optimal three-dimensional mesh using SVV parameters suggested by the theory. Because of the computational expense associated with our three-dimensional simulations no specific attempt was made to reach a higher value of Weissenberg number, as for example in [3].

In addition to the drag correction factor we also computed the stress profiles along the front and rear centerlines and on the sphere surface, following the recommendations in [5,34]. These profiles are representative of how well the stress wake is resolved. In Fig. 17 we plot the axial normal stress along the axis of symmetry and the sphere surface and we compare with the results of Fan et al. [5]. The value

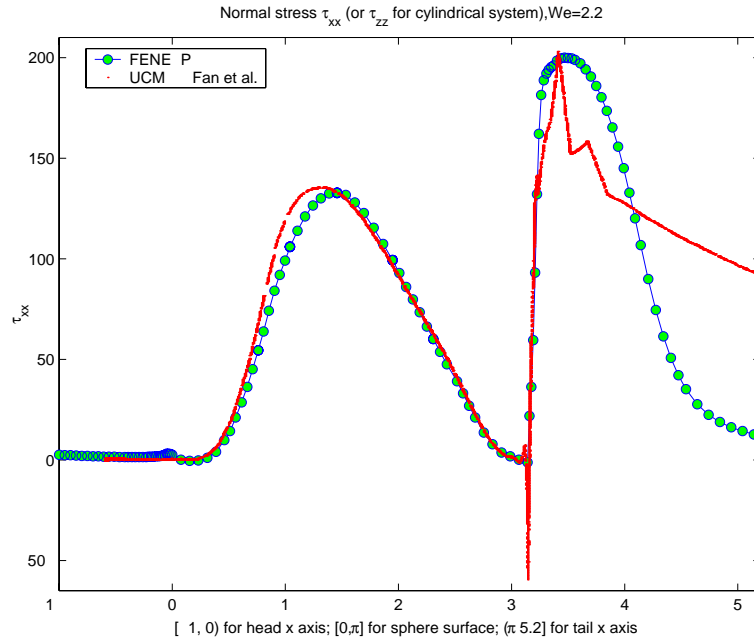


Fig. 17. Profiles of the axial normal stress along the axis of symmetry and the surface of the sphere. Here 0 in the horizontal axis corresponds to the front stagnation point and  $\pi$  the rear stagnation point,  $We = 2.2$ .

of Weissenberg number is  $We = 2.2$  in this case which is the maximum value reached in the work of Fan et al. As it is pointed out in their work, their stress profile seems to be inaccurate despite the fact that the drag correction factor at  $We = 2.2$  agrees with the values in the literature. The FENE-P predictions seem accurate; at lower values of  $We$  our results are in good agreement with the results of Fan et al.

## 5. Flow past a 3D ellipsoid at high Reynolds number

Next we consider external flow past a three-dimensional ellipsoid, i.e. a non-axi-symmetric body as shown in the mesh plot in Figs. 18 and 19. In particular, uniform inflow is considered past an ellipsoid with axes dimensions  $4 \times 2 \times 6$  length units. Both steady and unsteady cases were simulated. In the steady case the domain extends from  $[-12, 12]$  in the  $x$ -direction (flow direction),  $[-4, 4]$  in the  $z$ -direction (vertical direction), and  $[-6, 6]$  in the spanwise  $y$ -direction. For the unsteady case, the domain extends to  $[-16, 32]$  units in the flow direction. The number of elements is 640 in the steady case and 624 in the unsteady case; the spectral order was  $N = 6$  for all cases. The distribution of the elements size is very different in the two cases; in the unsteady case this distribution has been optimized based on the lessons learned from the steady case, for which the resolution was excessive. The boundary conditions imposed for the conformation tensor upon inflow are as described in Section 4 for the sphere problem.

We have simulated four different cases at Reynolds number  $Re = 93.4, 565$  (steady), and  $Re = 848, 1075$  (unsteady). The Reynolds number definition is based on the *geometric mean* of the two ellipsoid axes in the crossflow plane. We have also simulated  $We = 0.1$  and  $0.2$ . The parameter  $L$  throughout this

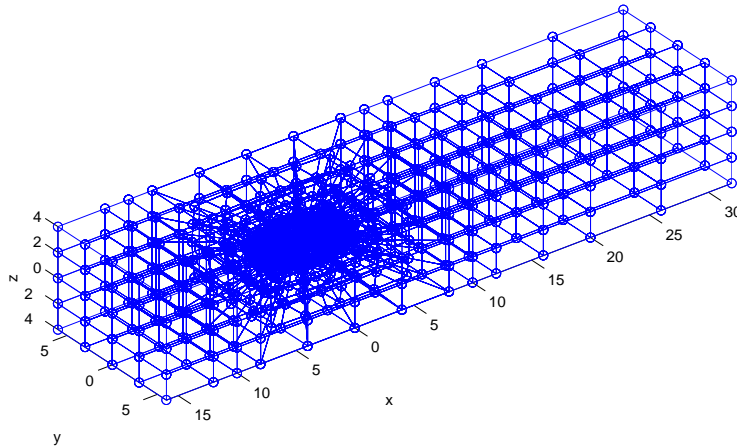


Fig. 18. Three-dimensional domain for simulating flow around a 3D ellipsoid.

section is set to the value of 10, the time step  $\Delta t = 5E-4$  and the SVV parameters are  $\varepsilon = 0.0001$  and  $M = 2$ .

We first report results for the steady case at  $Re = 93.4$ . In Table 4 we present the values of the drag coefficient normalized as follows

$$C_d = \frac{F_x}{0.5\rho U^2 D_y D_z},$$

where  $D_y$  and  $D_z$  are the axes in the crossflow  $y$  and  $z$  directions. We see that there is a substantial drag reduction even in steady state in the case of the FENE-P fluid ( $\beta \neq 1$ ) compared to the Newtonian fluid ( $\beta = 1$ ) at similar conditions. As a rough estimate of the shear-thinning effect, in Table 4 we also present the Newtonian results of the corresponding lower viscosity parameter.

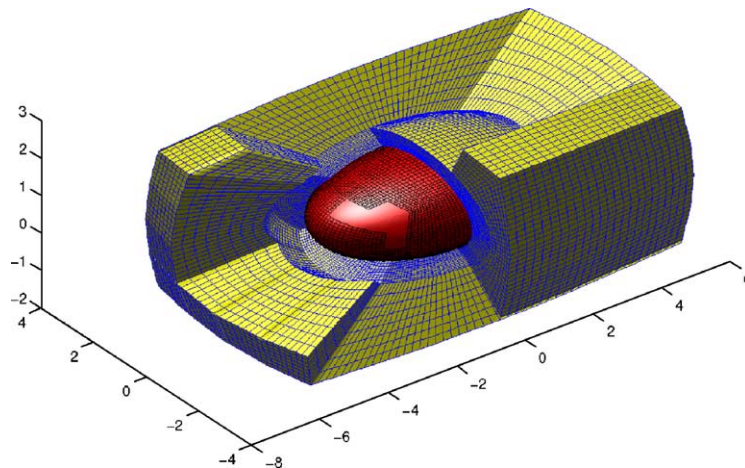


Fig. 19. Detail of the mesh around the 3D ellipsoid.

Table 4  
 Drag coefficient for steady laminar flow past a 3D ellipsoid;  $Re = 93.4$  (upper) ( $L = 10$ )

	Case			
	$\beta = 1$	$\beta = 0.8$	$\beta = 0.5$	$\beta = 0.8$
$C_d$	0.597	0.469 (-21.4), $We = 1.1$	0.368 (-38.4), $We = 1.1$	0.441 (-26.2), $We = 2.5$
$C_d$		0.523 (-12.4), $We = 0.0$	0.418 (-30.0), $We = 0.0$	

The numbers in parentheses denote percentage difference with respect to the Newtonian case corresponding to  $\beta = 1$ . Here we also include the Newtonian results with lower viscosity (lower).

In Fig. 20 we plot the quantitative differences of the surface stress along two different directions and show explicitly the contribution due to polymer. The model parameters are  $\beta = 0.8$  and Weissenberg number  $We = 1.1$ . In Fig. 21 we plot the streamwise velocity for the two fluids. The plot in the wake region on the right shows that the separation bubble is larger for the Newtonian fluid.

In Fig. 22 we plot the time-history of the streamwise velocity component at one point in the near-wake at  $Re = 848$ . Specifically, the point is located at  $x = 6.2, y = 0, z = 0$ . We compare both FENE-P and Newtonian flows. We first observe that a steady periodic state is achieved, i.e. a three-dimensional limit cycle for both cases. However, the frequency content is higher for the FENE-P fluid with pronounced super-harmonics. Also, the main Strouhal frequency is somewhat higher for the FENE-P compared to the Newtonian case. In Fig. 23 we plot the time-history of a near-wake point at  $Re = 1075$ . Specifically, the point is located at  $x = 4.59730021, y = -1.65243340, z = 0.0$ . From the corresponding frequency spectrum we see that the flow at this Reynolds number is in the early turbulent regime.

In Fig. 24 we plot the quantitative differences of the surface stress for the three larger values of Reynolds number, and in Fig. 25 we show differences in profiles of the corresponding surface pressure. The former is substantial whereas the latter is relatively small.

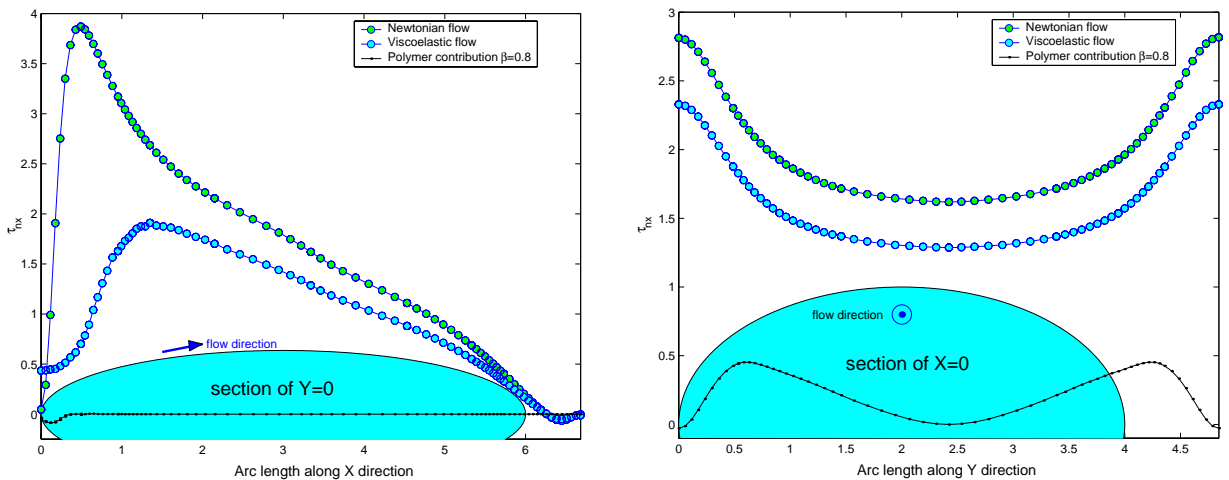


Fig. 20. Comparisons of the surface stress (axial normal) at two different planes:  $Re = 93.4$  and  $\beta = 0.8$ .

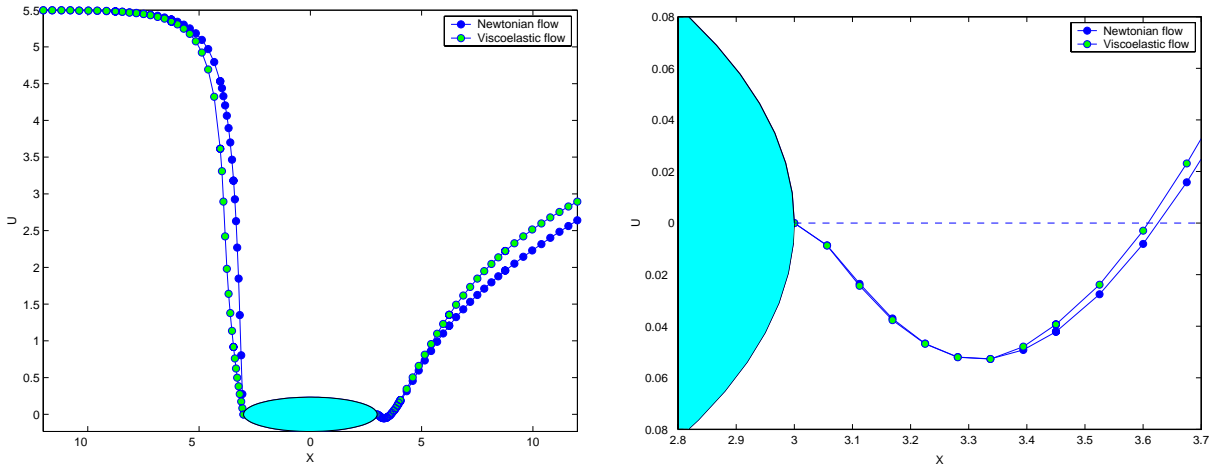


Fig. 21. Comparison of streamwise velocity profiles along the flow centerline, zoom in the wake (right):  $Re = 93.4$  and  $\beta = 0.8$ .

In Fig. 26 we plot the quantitative differences of the surface stress for different Weissenberg number, and in Fig. 27 we show differences in the profiles of the corresponding surface pressure. The Reynolds number is maintained constant at  $Re = 848$  and the coupling parameter is  $\beta = 0.9$ . Here both surface stress and surface pressure are substantially influenced by the value of the Weissenberg number. Note that the separation points move downstream as the Weissenberg number increases (Fig. 26).

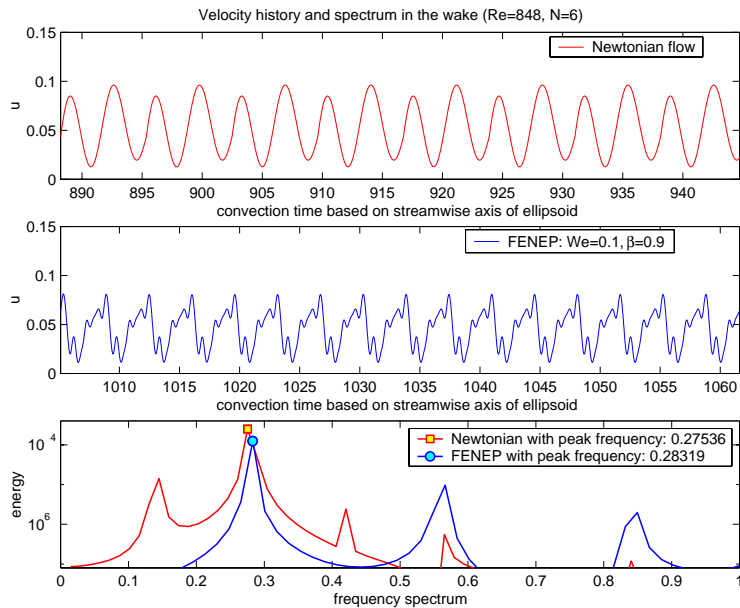


Fig. 22. Time-history and corresponding frequency spectra of streamwise velocity component for a near-wake point: upper—Newtonian, lower—FENE-P,  $Re = 848$ .

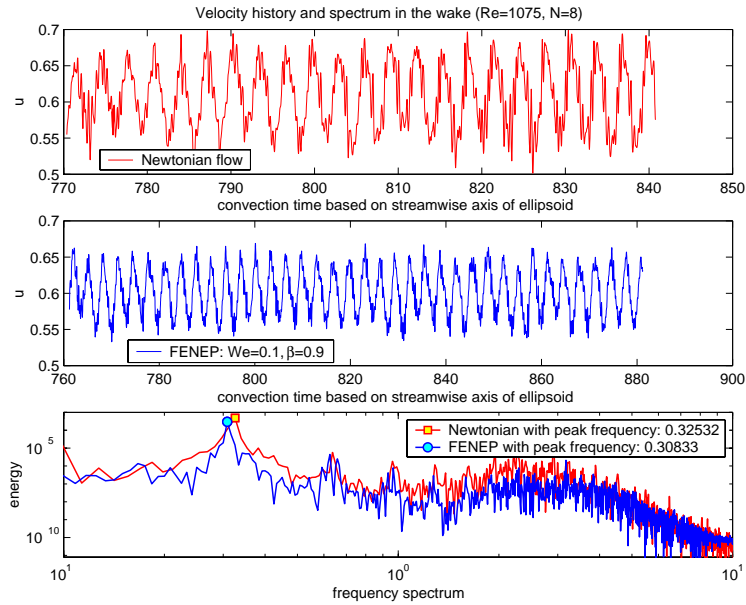


Fig. 23. Time-history and corresponding frequency spectra of streamwise velocity component for a near-wake point: upper—Newtonian, lower—FENE-P,  $Re = 1075$ .

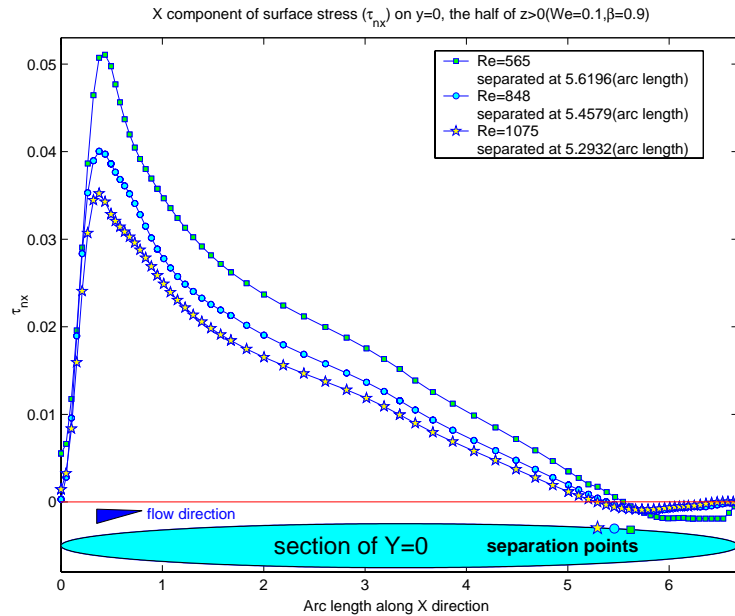


Fig. 24. Effect of Reynolds number on the surface stress at  $We = 0.1$  and  $\beta = 0.9$ .

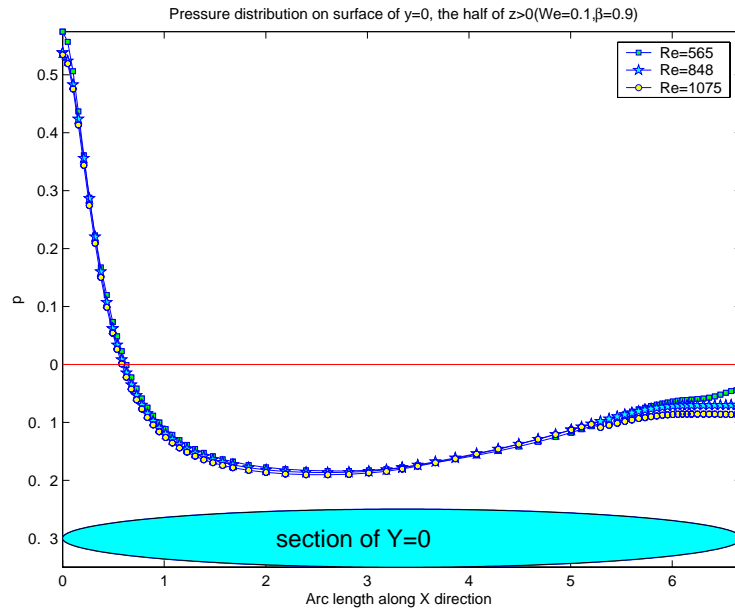


Fig. 25. Effect of Reynolds number on the surface pressure at  $We = 0.1$  and  $\beta = 0.9$ .

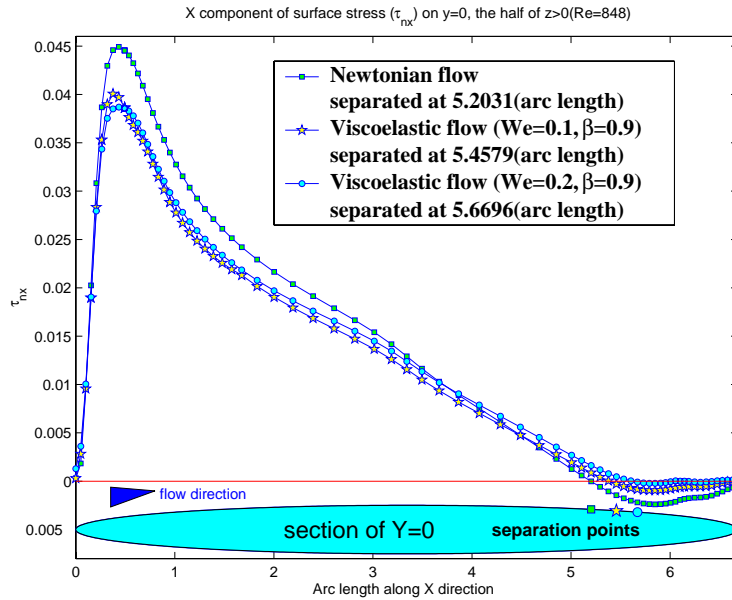


Fig. 26. Effect of Weissenberg number on the surface stress at  $Re = 848$ . Note the separation points on the ellipsoid surface.

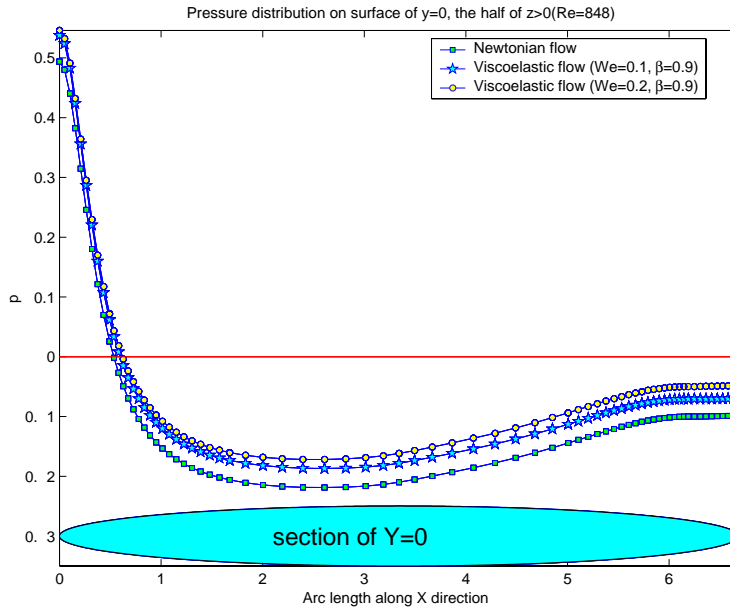


Fig. 27. Effect of Weissenberg number on the surface pressure at  $Re = 848$ .

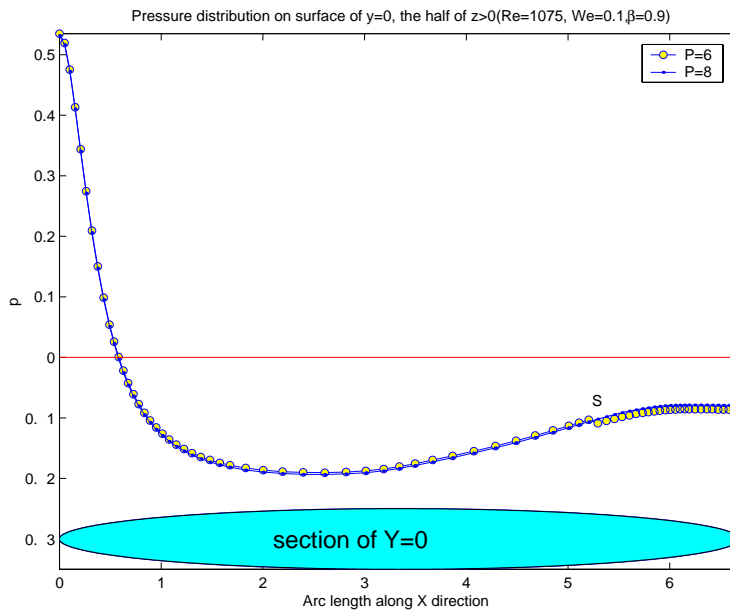


Fig. 28. Pressure profiles at  $N = 6$  and  $8$  for  $Re = 1075$  and  $We = 0.1$ . Note the sudden change in pressure at the separation point  $S$  in the low resolution case. See also Fig. 24.

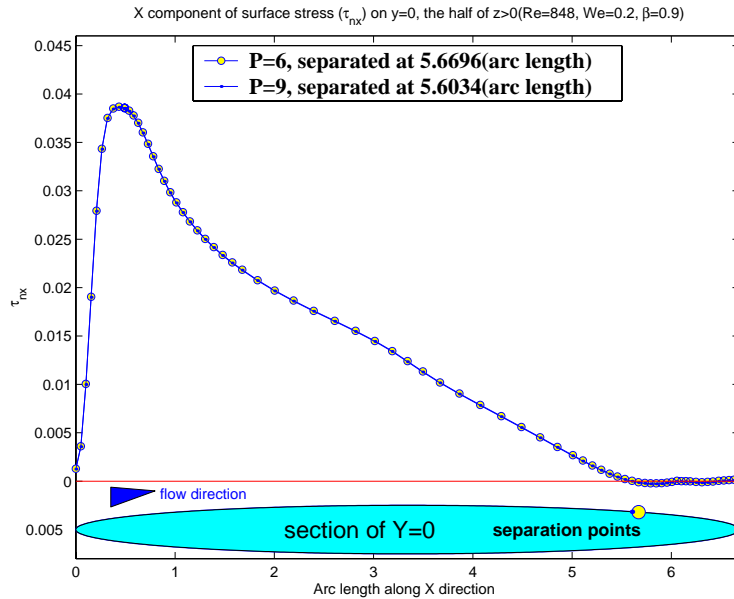


Fig. 29. Stress profiles and separation points at  $N = 6$  and  $9$  for  $Re = 848$  and  $We = 0.2$ .

Finally, we have performed systematic  $p$ -refinement studies to assess the accuracy of the results presented here for flow around the three-dimensional ellipsoid. We report here only representative results for the two higher Reynolds number  $Re = 1075$  with  $We = 0.1$  and  $Re = 875$  with  $We = 0.2$ .

For  $Re = 1075$  the root mean square (rms) fluctuations of the velocity histories shown in Fig. 23 are 0.03143 for  $N = 6$  and 0.03143 for  $N = 8$  for the non-Newtonian flow. The corresponding values for the Newtonian flow are 0.04361 and 0.04360 for the two resolutions. This shows that the flow seems to be well-resolved at the highest Reynolds number we considered in this work and also that the polymer reduces somewhat the streamwise fluctuations. Examination of other quantities show similar results. In Fig. 28 we show the pressure distribution for the two resolutions. We see some small deviation, especially in the wake; this was the largest deviation that we could detect in comparing the two runs at  $N = 6$  and  $8$ .

Next we present a representative comparison for the  $Re = 848$  with  $We = 0.2$  case in Fig. 29. We performed runs with resolution  $N = 6$  and  $9$ . We see that there is no visible difference in the stress distribution although we observed the separation point moving slightly downstream in the higher resolution case.

## 6. Summary

We have presented a new numerical method suitable for simulating high Reynolds number viscoelastic flows. Our particular interest is on turbulent drag reduction for flows around hydrodynamic surfaces (e.g. ship hulls, torpedos, etc.) using polymers, and some of the developments in this paper were motivated by this application. To this end, the modified splitting scheme proposed in [22] in combination with the modal type representation of spectral elements has been found to be both robust and accurate. We have been following this procedure for Newtonian turbulent flows with success as well, e.g. see [36]. In the benchmark

problems, we intentionally targeted three-dimensional configurations in order to demonstrate that spectral element simulations are practical and that the new stabilization technique is quite effective. Moreover, the Weissenberg number  $We = 2.0$  reached in the two-dimensional flow past a cylinder, together with the smoothness of the  $T_{xx}$  profiles for these Weissenberg numbers, demonstrate the stability of the method.

The use of numerical diffusion to stabilize simulations of hyperbolic nature goes back to von Neumann and Richtmyer, and it has been practiced routinely in aerodynamic flows, and also in subgrid scale models in large-eddy simulations. However, in more recent work it has been formulated as an adaptive feature, i.e. to be used non-uniformly in space and/or in time as needed. In addition, high-order superviscosity kernels have been the preferred choice. In viscoelastic flows, explicit treatment with artificial viscosity has been done typically without a particularly close connection to resolution or the spatial non-uniformities in the stress field. Of course, formulations such as SUPG address this issue implicitly, but here we refer to explicit artificial viscosity approaches. The current formulation addresses that by targeting modal representations of the numerical solution. We have introduced the spectral vanishing viscosity method that imposes monotonicity of the solution without affecting the lower most energetic modes. Only the upper one-third of the modes is affected in a special way so that the high-order accuracy (exponential in our case here) is maintained.

The appeal of the new approach is that it derives its origin in non-linear hyperbolic laws—a theoretical proof presented first by Tadmor [15]. Another useful feature from the implementation standpoint is that the convolution kernel that represents SVV is second-order and thus it can be easily implemented in existing finite element codes. To this end, an extension of the method in the physical (instead of modal) domain is required but some initial work has already been done in [25].

This is the first paper using SVV for viscoelastic flows and many issues need to be resolved. First, the two parameters that characterize the SVV kernel, namely the amplitude and cut-off wavenumber need to be studied more systematically. In the presented examples we have seen that the values of the viscosity amplitude  $\varepsilon$  depend on the flow parameters. Our criterion in choosing  $\varepsilon$  has been to employ the smallest value that ensures stability since this will not decrease the accuracy.

A dynamic model that relates the amplitude of SVV and the local strain needs to be explored and implemented appropriately. In addition, the smooth kernel  $Q(M, N)$  can be modified so that a space-dependent (i.e. variable) cut-off wavenumber be introduced. Finally, more tests are required in the context of other viscoelastic models in addition to the FENE-P considered here.

## Acknowledgements

The authors would like to thank Dr. Cédric Chauvière for his help and for providing his results on the FENE-P model. We would also like to thank Dr. K. Housiadas and Prof. A. Beris for useful discussions. This work was supported by DARPA and by NSF.

## References

- [1] A.N. Beris, R.C. Armstrong, R.A. Brown, Spectral/finite-element calculations of the flow of a Maxwell fluid between eccentric rotating cylinders, *J. Non-Newtonian Fluid Mech.* 22 (1987) 129–167.
- [2] R.G. Owens, T.N. Phillips, *Computational Rheology*, Imperial College Press, 2002.
- [3] J. Petera, A new finite element scheme using the Lagrangian framework for simulation of viscoelastic fluid flows, *J. Non-Newtonian Fluid Mech.* 103 (2002) 1–43.

- [4] R.M. Phillips, T.N. Phillips, Flow past a cylinder using a semi-Lagrangian spectral element method, *Appl. Numer. Math.* 33 (2000) 251–257.
- [5] Y. Fan, R.I. Tanner, N. Phan-Thien, Galerkin/least-square finite element methods for steady viscoelastic flows, *J. Non-Newtonian Fluid Mech.* 84 (1999) 233–256.
- [6] C. Chauvière, R.G. Owens, A new spectral element method for the reliable computation of viscoelastic flow, *Comput. Methods Appl. Mech. Eng.* 190 (2001) 3999–4018.
- [7] M.A. Hulsen, A.P.G. van Heel, B.H.A.A. van den Brule, Simulation of viscoelastic flows using brownian configuration fields, *J. Non-Newtonian Fluid Mech.* 70 (1997) 79–101.
- [8] H.R. Warner, Kinetic theory and rheology of dilute suspensions of finitely extensible dumbbells, *Ind. Eng. Chem. Fundam.* 11 (1972) 379–387.
- [9] A.P.G. van Heel, M.A. Hulsen, B.H.A.A. van den Brule, On the selection of parameters in the FENE-P model, *J. Non-Newtonian Fluid Mech.* 75 (1998) 253–271.
- [10] R. Sureshkumar, A.N. Beris, R.A. Handler, Direct numerical simulation of turbulent channel flow of a polymer solution, *Phys. Fluids* 9 (1997) 743–755.
- [11] C.D. Dimitropoulos, R. Sureshkumar, A.N. Beris, Direct numerical simulation of viscoelastic turbulent channel flow exhibiting drag reduction: effect of the variation of rheological parameters, *J. Non-Newtonian Fluid Mech.* 79 (1998) 433–468.
- [12] A.N. Beris, B.J. Edwards, *Thermodynamics of Flowing Systems with Internal Microstructure*, Oxford University Press, New York, 1994.
- [13] C. Chauvière, *Stabilized spectral element methods for the simulation of viscoelastic flows*, Ph.D. Thesis, Lausanne, EPFL, 2002.
- [14] G.E. Karniadakis, S.J. Sherwin, *Spectral/hp Element Methods for CFD*, Oxford University Press, New York, 1999.
- [15] E. Tadmor, Convergence of spectral methods for nonlinear conservation laws, *SIAM J. Numer. Anal.* 26 (1) (1989) 30.
- [16] G.-S. Karamanos, G.E. Karniadakis, A spectral vanishing viscosity method for large-eddy simulations, *J. Comput. Phys.* 162 (2000) 22–50.
- [17] S.M. Ould Kaber, A Legendre pseudospectral viscosity method, *J. Comput. Phys.* 128 (1996) 165.
- [18] Ø. Andreassen, I. Lie, C.E. Wasberg, The spectral viscosity method applied to simulation of waves in a stratified atmosphere, *J. Comput. Phys.* 110 (1994) 257.
- [19] E. Tadmor, Super viscosity and spectral approximations of nonlinear conservation laws, in: M.J. Baines, K.W. Morton (Eds.), *Numerical Methods for Fluid Dynamics*, vol. IV, Clarendon Press, Oxford, 1993, p. 69.
- [20] H.-P. Ma, Chebyshev–Legendre spectral viscosity method for nonlinear conservation laws, *SIAM J. Numer. Anal.* 35 (3) (1998) 901.
- [21] H.-P. Ma, Chebyshev–Legendre super spectral viscosity method for nonlinear conservation laws, *SIAM J. Numer. Anal.* 35 (3) (1998) 903.
- [22] G.E. Karniadakis, M. Israeli, S.A. Orszag, High-order splitting methods for incompressible Navier–Stokes equations, *J. Comput. Phys.* 97 (1991) 414.
- [23] G.-S. Karamanos, C. Evangelinos, R.M. Kirby, G.E. Karniadakis, DNS of turbulence on a PC/Linux cluster: fact or fiction, in: *Proceedings of the Supercomputing, 1999*.
- [24] M.G. Crandall, P.L. Lions, Viscosity solutions of Hamilton–Jacobi equations, *Trans. Am. Math. Soc.* 61 (1983.) 629.
- [25] Y. Maday, S.M. Ould Kaber, E. Tadmor, Legendre pseudospectral viscosity method for nonlinear conservation laws, *SIAM J. Numer. Anal.* 30 (1993) 321.
- [26] E. Tadmor, Total variation and error estimates for spectral viscosity approximations, *Math. Comput.* 60 (1993) 245.
- [27] R.M. Kirby, *Toward dynamic spectral/hp refinement: algorithms and applications to flow-structure interactions*, Ph.D. Thesis, Brown University, 2003.
- [28] R.H. Kraichnan, Eddy viscosity in two and three dimensions, *J. Atmos. Sci.* 33 (1976) 1521.
- [29] M. Lesieur, O. Metais, New trends in large-eddy simulation, *Ann. Rev. Fluid Mech.* 28 (1996) 45.
- [30] J.P. Chollet, Two-point closures as a subgrid scale modelling for large eddy simulations, in: F. Durst, B. Launder (Eds.), *Turbulent Shear Flows*, vol. IV, Lecture Notes in Physics, Springer, Berlin, 1984.
- [31] C. Chauvière, R.G. Owens, A robust spectral element method for simulations of time-dependent viscoelastic flows, *J. Sci. Comput.* 17 (2002) 191–199.
- [32] M.J. Crochet, Y.R. Fan, High-order finite element methods for steady viscoelastic flows, *J. Non-Newtonian Fluid Mech.* 57 (1995) 283–311.

- [33] Y.R. Fan, A comparative study of the discontinuous Galerkin and continuous SUPG finite element methods for computation of viscoelastic flows, *Comput. Methods Appl. Mech. Eng.* 141 (1997) 47–65.
- [34] F.P. Baaijens, S.H. Selen, H.P. Baaijens, G.W. Peters, H.E. Meijer, Viscoelastic flow past a confined cylinder of a low density polyethylene melt, *J. Non-Newtonian Fluid Mech.* 68 (1997) 173–203.
- [35] M.B. Bush, On the stagnation flow behind a sphere in a shear-thinning viscoelastic liquid, *J. Non-Newtonian Fluid Mech.* 55 (1994) 229–247.
- [36] X. Ma, G.-S. Karamanos, G.E. Karniadakis, Dynamics and low-dimensionality of the turbulent near-wake, *J. Fluid Mech.* 410 (2000) 29–65.